Title	A Neural Network Interatomic Potential for the Ternary α-Fe-C-H System: Toward Million-Atom Simulations of Hydrogen Embrittlement in Steel
Author(s)	Meng, Fan Shun; Shinzato, Shuhei; Matsubara, Kazuki et al.
Citation	JOM. 2025, 77(11), p. 8101-8117
Version Type	VoR
URL	https://hdl.handle.net/11094/103272
rights	This article is licensed under a Creative Commons Attribution 4.0 International License.
Note	

A Neural Network Interatomic Potential for the Ternary α-Fe-C-H System: Toward Million-Atom Simulations of Hydrogen Embrittlement in Steel

FAN-SHUN MENG [ORCID],[1,4] SHUHEI SHINZATO,[1] KAZUKI MATSUBARA,[2] JUN-PING DU,[1] PEIJUN YU,[3] and SHIGENOBU OGATA[1,5]

1.—Department of Mechanical Science and Bioengineering, Graduate School of Engineering Science, The University of Osaka, 1-3 Machikaneyama, Toyonaka, Osaka 560-8531, Japan. 2.—Steel Research Laboratory, JFE Steel Corporation, Kawasaki 210-0855, Japan. 3.—School of Materials Science and Technology, Hainan University, Haikou 368721, China. 4.—e-mail: fanshun.meng@tsme.me.es.osaka-u.ac.jp. 5.—e-mail: ogata.shigenobu.es@osaka-u.ac.jp

A neural network interatomic potential (NNIP) has been developed for the ternary system of α-iron, carbon, and hydrogen to clarify the degradation behavior of Fe-C steels in hydrogen-rich environments. The NNIP was trained on an extensive reference database generated from spin-polarized density functional theory (DFT) calculations. It demonstrates remarkable performance in various scenarios relevant to Fe and Fe-C systems under hydrogen, including the diffusion kinetics of H and C in Fe and their thermodynamic interactions with iron vacancies, grain boundaries, screw dislocations, cementite, and cementite–ferrite interfaces. Using this NNIP, we conducted large-scale (one-million-atom) molecular dynamics (MD) simulations of uniaxial tensile tests on C-containing α-Fe both with and without H, showing that hydrogen enhances defect accumulation during plastic deformation, which may eventually lead to material failure.

INTRODUCTION

Fe-C steels are widely used in modern infrastructure but often suffer from premature failure in hydrogen-containing environments. Consequently, understanding the fundamental interactions among Fe, C, and H is crucial for mitigating hydrogen-induced degradation. In pursuit of this goal, numerous efforts have focused on developing empirical interatomic potentials (EIPs) for iron-based systems (e.g., Fe,[1,2] Fe-H,[3,4] and Fe-C[5,6]) in various formalisms, significantly advancing our understanding of hydrogen embrittlement (HE)[7] and the role of carbon in the mechanical properties of iron.[8] One common approach to developing potentials for

multi-element systems is to combine or hybridize existing EIPs. For instance, the Fe-C embedded atom method (EAM) potential by Restrepo et al.[9] was built by merging EAM potentials for Fe[1] and Fe-C.[5] For the Fe-C-H ternary system, Zhou et al.[10] constructed two bond-order potentials by integrating potentials for Fe-H, Fe-C, and C-H, successfully applying them to studies of hydrogen distribution in Fe-C steels.[11] Similarly, Mun et al.[12] proposed a modified EAM (MEAM) potential by combining MEAM potentials for Fe-C,[13] Fe-H,[14] and a bond-order-based MEAM (MEAM-BO) potential for C-H.[15] This allowed them to capture various alkane molecules, vacancy–H/C interactions, and basic cementite properties. Another example is the ReaxFF reactive force field, initially developed for hydrogen adsorption and dissociation on iron and iron-carbide surfaces,[16] which, after refitting the Fe-C interaction parameters, could describe hydrogen behavior in nano-voids and at ferrite–cementite interfaces.[17]

The advantage of such combination or hybridization strategies is that they preserve key properties from each component EIP. A prime example is the EAM potentials developed by Mendelev et al.[1] and Ackland et al.,[2] which have been widely adopted and extended for iron-based systems largely because they correctly capture the compact core structure of screw dislocations. However, undesirable features can also be preserved. For instance, the Fe-H EAM potential by Ramasubramaniam[3] introduced an unphysical double-hump feature during vacancy-H diffusion,[18] an inherited artifact from Mendelev's Fe EAM potential.[1] In short, the accuracy of such hybridized multi-element potentials strongly depends on the quality of each underlying component. Moreover, even a comprehensive refitting of a large database does not guarantee accurate reproduction of all relevant properties, because classical functional forms impose inherent limitations. By contrast, recent progress in machine learning interatomic potentials[19,20] exploit the flexibility of machine learning to achieve near ab initio accuracy at a substantially lower computational cost,[21] and significant contributions have been made in improving our understanding of microscopic mechanisms of deformation and phase transitions in various materials.[22–24]

In this work, we present a high-accuracy and highly transferable neural network interatomic potential (NNIP) for the α-Fe-C-H ternary system. This potential was trained on an extensive database generated by spin-polarized density functional theory (DFT) calculations. It achieves near-DFT accuracy for α-Fe, Fe_3C, and the interactions of C and/or H with both pristine and defective α-Fe, including vacancies, surfaces, grain boundaries, screw dislocations, and cementite–ferrite-carbide interfaces. Using this NNIP, we conducted large-scale (one-million-atom) molecular dynamics (MD) simulations of uniaxial tensile tests on C-containing α-Fe with and without H, demonstrating both its excellent transferability and reliability, and showing that H accelerates vacancy accumulation during plastic deformation in steel.

METHODOLOGY

Neural Network Interatomic Potential

The NNIPs were trained under the framework of the neural network potential package ($n2p2$).[25] To parameterize the local atomic environments of the configurations in a reference database, radial and angular atom-centered symmetry functions (ACSFs)[26] were adopted. The radial symmetry function is defined as:[26]

$$G_I^{\mathrm{rad}} = \sum_j e^{-\eta(R_{ij}-R_s)^2} f_c(R_{ij}), \tag{1}$$

where R_{ij} is the atomic distance between an atom, j, and the central atom, I. The angular symmetry function is given by:[26]

$$G_I^{\mathrm{ang-w}} = 2^{1-\xi}\sum_j\sum_{k\neq j}(1+\lambda\cos\theta_{ijk})^\xi e^{-\eta(R_{ij}+R_{ik})^2} f_c(R_{ij})f_c(R_{ik}), \tag{2}$$

and:

$$G_I^{\mathrm{ang-n}} = 2^{1-\xi}\sum_j\sum_{k\neq j}(1+\lambda\cos\theta_{ijk})^\xi e^{-\eta(R_{ij}^2+R_{ik}^2+R_{jk}^2)} f_c(R_{ij})f_c(R_{ik})f_c(R_{jk}), \tag{3}$$

where θ_{ijk} is the angle enclosed by the vectors of R_{ij} and R_{ik} of two neighboring atoms, j and k, respectively. Both types of ACSF have a common function f_c called the cutoff function, which is defined as:

$$f_c(R_{ij}) = \begin{cases} \tanh^3[1-\frac{R_{ij}}{R_c}] & \mathrm{if} R_{ij} \leq R_c \\ 0.0 & \mathrm{if} R_{ij} > R_c, \end{cases} \tag{4}$$

The parameters of η, R_s, ξ, and λ in Eqs. 1–3 can be determined by the strategy reported in Ref. 27. Each element has 24 radial and 120 (96 $G_I^{\mathrm{ang-w}}$ +24 $G_I^{\mathrm{ang-n}}$) angular ACSFs. The cutoff radii R_c for radial and angular ACSFs are 6.5 and 6.0 Å for Fe, 6.0 and 5.0 Å for C, and 3.8 and 3.6 Å for H, respectively. These settings result in an average number of neighbors of 106 for Fe, 73 for C, and 18 for H, as determined from the structures in the training dataset.

Training Data Set

To construct a potential which can widely used for the studies of α-Fe, α-Fe-C (including cementite), α-Fe-H, and α-Fe-C-H systems, our primary focus is on the interactions of hydrogen and/or carbon atoms with defective iron (vacancies, surfaces, grain boundaries, screw dislocation), and hydrogen with cementite and the ferrite–cementite interface. Of course, the NNIP should also be able to make a reasonable description of the basic properties of the α-iron and cementite. With these considerations, a comprehensive reference database were prepared by using spin-polarized DFT) calculations, which included three datasets: unary systems of α-Fe, C, H_2, binary systems of α-Fe-H, α-Fe-C, and a ternary system of α-Fe-C-H. A few of configurations related to methane molecules (CH_4) were also included. The rule of the dataset generation is presented in the Supplementary Materials (Note 1). Note that the same settings should be used for all the DFT calculations to sustain the data compatibility or a high error should be expected. Details of the DFT calculation settings can be found in our previous work.[28] In total, 62,743 configurations, equivalent to 6.05×10^6 atomic environments, were prepared in the database. These structures were distributed randomly into a training dataset (90%) and a testing dataset (10%). Both energy and atomic force were all considered in the training processes.

All DFT calculations were completed using Vienna Ab-initio Simulation Package.[29] The potential validation and application were carried out by the Large-scale Atomic/Molecular Massively Parallel Simulator (LAMMPS).[30,31] Simulation visualization and atomistic figures plot are completed with the help of OVITO.[32] Additionally, the PHONOPY code[33] was used to calculate the phonon dispersion curves of various systems, the code of Atomsk[34] was employed to build screw dislocation models, and the climbing image nudged elastic band method[35] was adopted to find the energy barrier between two states.

RESULTS: VALIDATION OF THE NNIP

The overall accuracy of the NNIP was estimated using the root mean squared error (RMSE) of energies (E) and forces (F) the definition of which can be found elsewhere.[36,37] The training and testing datasets have RMSE(E)s of 3.17 meV/atom and 3.11 meV/atom, and RMSE(F)s of 92.6 meV/Å and 93.1 meV/Å, respectively. The point by point comparison of DFT and NNIP produced energies and forces of the structures in the training and testing datasets are supplied in the Supplementary Materials (see Fig. S1). The values of these RMSEs are in the typical range of machine learning based interatomic potentials,[21,38] and the small difference between these RMSEs of training and testing datasets denotes that no overfitting occurred.[39] Several concerned properties are further confirmed in the following subsections.

NNIP Performance for Pure α-iron

The NNIP performance for the basic properties of α-Fe, including lattice constant, elastic constants, defects formation energies, and low index surface energies, are tabulated in Table S1 in the Supplementary Materials. All of them show the similar performance as our previous α-Fe-H[28] and α-Fe-C NNIPs,[40] and agree well with the DFT results.[41–46]

The phonon dispersion curve of pure α-Fe with equilibrium lattice condition is presented in Fig. 1a, frm which it is clear that the NNIP can reproduce the DFT[47] and experimental results well.[48] The linear thermal expansion coefficients at finite temperatures, as obtained from the NNIP and compared with experimental data, are presented in Fig. S2 of the Supplementary Materials.

The relationship between misorientation and formation energy of symmetric tilt grain boundaries (GBs) with the tilt axis of ⟨110⟩ is shown in Fig. 1b. The NNIP can well reproduce the trained data and also can precisely predict the energies of the unseen GBs, as compared with the DFT results.[49–51] The above good transferability of the NNIP is also presented in the cases of the symmetric tilt GBs with tilt axes of ⟨001⟩ and ⟨111⟩, and twist GBs with rotation axes of ⟨001⟩, ⟨110⟩ and ⟨111⟩, which are provided in the Supplementary Materials (see Fig. S3).

The energy responds to the relative position of two halves of the crystal (i.e., γ-surface) of the (112) and (110) planes are reproduced and displayed in Fig. 1c and Fig. S4 in the Supplementary Materials. The NNIP results are quantitatively in line with the DFT results.[46]

The energetics of screw dislocation of α-iron is a long-term challenge for the empirical potentials, and many efforts have been dedicated to overcoming it.[47,52] A supercell with dimensions of $22[11\bar{2}] \times 38[1\bar{1}0] \times \frac{1}{2}[[111]$ was employed, and a periodic boundary condition was applied in the [111] direction only. A ½[111] screw dislocation was introduced according to the anisotropic elasticity theory of dislocation.[34] Three distinct core configurations, easy core, hard core, and split core, were created separately. Based on the energy of the easy core, the energies are 36.1 eV/b, 34.2 eV/b, and 108.0 eV/b (b is Burgers vector length, $\sqrt{3}/2 \times a_0$) for the hard core, middle point, and split core configuration, respectively. These results show good agreement with the DFT results of 39.3 meV/b, 37.9 meV/b, and 108 meV/b,[53] 57.9 meV/b, 49.2 meV/b, and 110.3 meV/b,[54] and the Fe-H NNIP result of 47.4 meV/b, 38.3 meV/b, and 82.3 meV/b and Fe-C NNIP result of 38.5 meV/b, 36.7 meV/b, and 110.9 meV/b, respectively The 2-dimensional Peierls energy mapped by NNIP is shown in Fig. 1d. It clear that there is only one hump between neighboring easy cores, and the whole shape vividly matches the reported DFT results.[55] With the help of a model containing a ½[111] screw dislocation with a length of 24b, the kink-pair nucleation enthalpy predicted by NNIP is 0.72 eV, which is in line with the results of the DFT–based line tension model of 0.73 eV,[53] 0.86 eV,[56] 0.91 eV,[57] and the α-Fe-H NNIP result of 0.7 eV.[28] Note that the core configurations are included in the database and others are not.

NNIP Performance for α-Iron with Hydrogen

The effects of the volumetric engineering strain (ε) to the solution energy (E_s^ε) and diffusion energy barrier (ΔE) of the H atom in α-Fe were examined using a $4 \times 4 \times 4$ α-iron supercell. The solution energy was obtained by: $E_s^\varepsilon = E_{\text{FeH}}^\varepsilon - E_{\text{Fe}}^\varepsilon - \frac{1}{2} E_{\text{H}_2}$, where $E_{\text{FeH}}^\varepsilon$ and $E_{\text{Fe}}^\varepsilon$ stand for the energies of pure α-Fe with a volumetric strain of ε with and without the H atom at the T site, respectively, E_{H_2} indicates the energy of an isolated H_2 molecule. As shown in Fig. 2a, E_s^ε decreased (increased) quickly as the strain increased (decreased), and it arrived at a value below 0 at the strain of 6.12%, which means that the hydrogen solubility in iron strongly depends on the strain. The strain effect to the hydrogen diffusivity is not significantly within the considered volumetric strain. Reported results
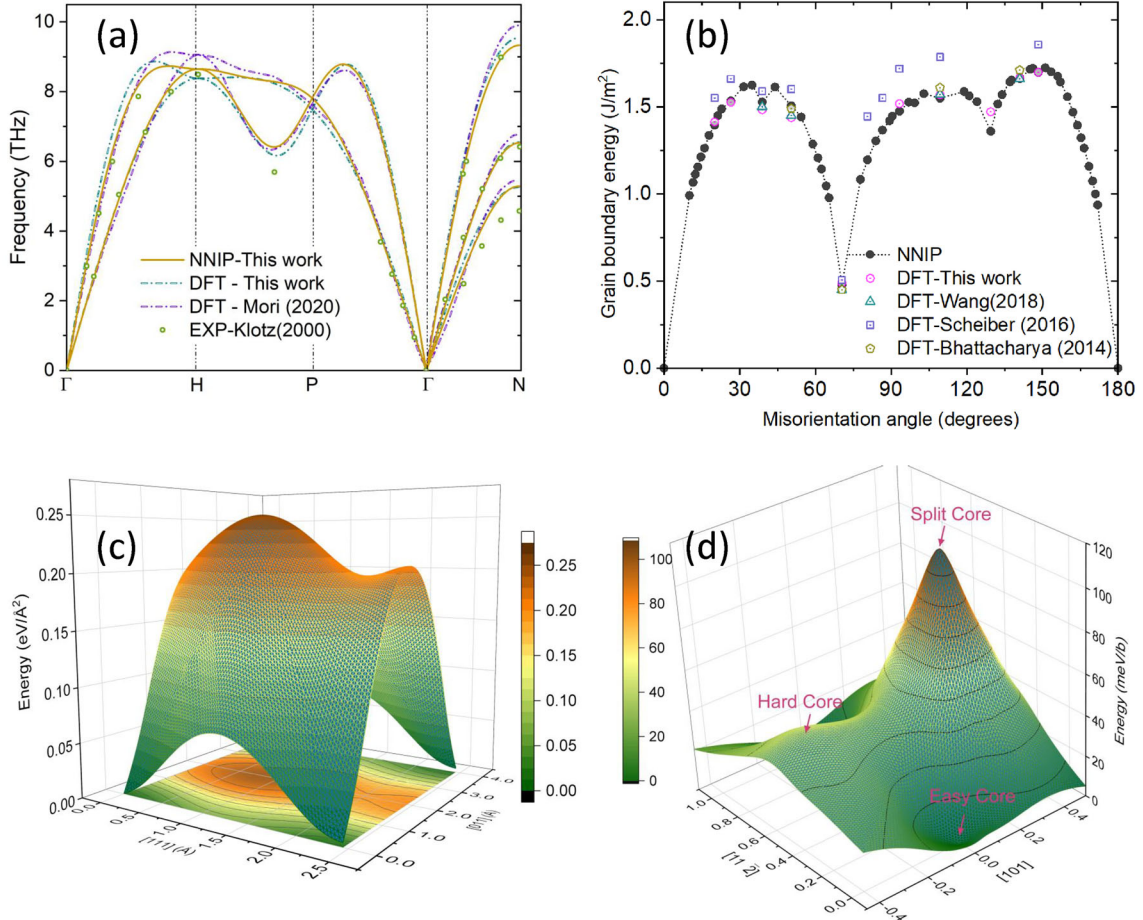
Fig. 1. NNIP performance for α-Fe: (a) phonon dispersion curve, (b) misorientation–energy relationship for the symmetric tilt GBs with a tilt axis of $\langle 110 \rangle$, (c) γ-surface for the $(11\bar{2})$ crystallographic plane, (d) 2-dimensional Peierls barrier of screw dislocation. The axes along [101] and $[11\bar{2}]$ directions in (d) are scaled by $\sqrt{3}/6a_0$; a_0 is the lattice constant of α-iron. The available reported DFT[47] and experimental[48] results for phonon dispersion curves and DFT results for symmetric tilt GB formation energy[49–51] are also shown.

based on DFT calculations are also plotted in the figure and a good agreement can be observed.[3]

The trapping energy of various number of H atoms in a monovacancy was also tested using a $4\times 4\times 4$ α-iron supercell with one vacancy. The trapping energy of the Ith H atom (E_{trap}^I) was determined by $E_{\mathrm{trap}}^I = (E_{\mathrm{Fe^{vac}H_I}} - E_{\mathrm{Fe^{vac}H_{(I-1)}}}) - (E_{\mathrm{Fe^{bcc}H_1}} - E_{\mathrm{Fe^{bcc}}})$,[18] where $E_{\mathrm{Fe^{vac}H_I}}$ and $E_{\mathrm{Fe^{vac}H_{(I-1)}}}$ stand for the energies of the vacancy containing I and $(I-1)$ H atoms, respectively, and $E_{\mathrm{Fe^{bcc}H_1}}$ and $E_{\mathrm{Fe^{bcc}}}$ indicate the energies of bcc Fe with and without one H atom at T-site. The corresponding configurations of different number of H atoms in a vacancy are shown in Fig. 2b. The NNIP shows that up to 5 H atoms can be accommodated by a monovacancy at T = 0 K, perfectly agreeing with the results of DFT calculations[58] and the α-Fe-H NNIP.[28]

The mechanical property degradation of metals introduced by H segregation at GBs is widely accepted. The configurations of hydrogen segregation at the $\Sigma5(310)[001]$ symmetric tilt GB and its influences on formation energy (γ_{GB}) and work of separation (γ_{wos}) are summarized in Fig. 2c and d,

respectively. For the formulae used for the computation of γ_{GB} and γ_{wos} , please refer to our previous work.[28] The presence of H atoms at the GB lowers its energy from 1.6 to 1.2 J/m^2 as H atoms are introduced gradually, indicating that the H-segregation stabilized the GB. However, the presence of H leads to the reduction in work of separation. The solution energies of various number of H atoms at the GB and their chemical/mechanical contributions can be found in the Supplementary Materials (see Table. S2). All of the above NNIP results show good agreement with the DFT calculations[59] and the same quality shown as the α-Fe-H NNIP.[28]

Recently, Borges et al.[60] reported that H atoms could stabilize the hard core configuration of the screw dislocation of α-Fe. The NNIP performance in the scenario was checked using a dipole screw dislocation model (see Fig. 2e). The current NNIP can well describe the stabilization. The core structure will automatically convert to the easy core configuration once the H-atom(s) is(are) tore off. NNIP obtained structural parameters for each case are shown, and the corresponding DFT results are

A Neural Network Interatomic Potential for the Ternary α-Fe-C-H System: Toward Million-Atom Simulations of Hydrogen Embrittlement in Steel
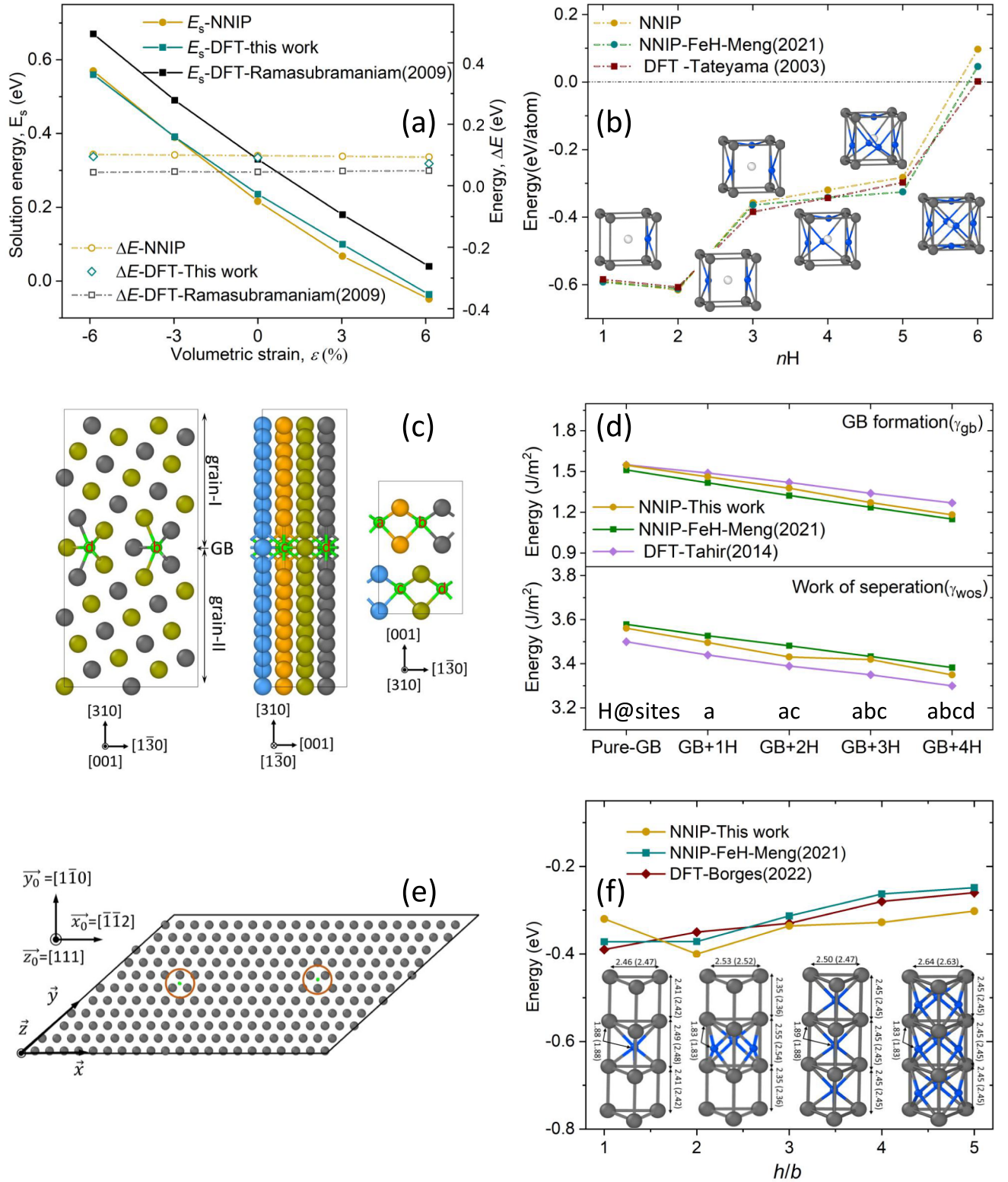

Fig. 2. NNIP performance for α-iron with hydrogen: (a) volumetric strain effects on solubility and diffusivity of H atom in α-iron, (b) local atomic configuration and trapping energy of various H atoms in monovacancy; the white ball stands for the vacancy. (c) Segregation sites in a symmetric tilt Σ5(310)[001] GB. (d) H influence on the formation energy and work of separation of the GB in (c), and (e) dipole screw dislocation model. (f) Interaction energy between the stabilized dislocation and 3H atoms; h stands for the dislocation length in the supercell. Each H-decorated core structure and its structural parameters (DFT results are provided in parentheses) are displayed in the inner panel. The second and the fourth H-decorated core structures corresponds to h/b = 3 and 1, respectively.

presented in parentheses. It is clear that all the above results show good agreement with our DFT verification. The interaction energy of 3 H atoms with separation of $1b$ (i.e., $h/b = 1$, corresponding to the most right configuration in the inner panel of Fig. 2f; h stands for the dislocation length of the model) with screw dislocation is -0.32 eV, which is slightly higher than that of the DFT result of -0.39 eV.[60] The interaction energy for the case of the 3 H with a separation of $2b$ ((i.e., $h/b = 2$) is about 0.08 eV lower than that of the $1b$ separation case, which differs from the reported DFT result (0.04 eV higher) but agrees with our own DFT result (0.12 eV lower). For other H-atom separations, NNIP presented good agreement with the reported DFT results.[60] The α-Fe-H NNIP[28] is also capable of correctly capturing the core configuration reconstruction induced by H atoms, and the corresponding interaction energies are also plotted in Fig. 2f.

NNIP Performance for α-Iron with Carbon and Cementite

Carbon atoms prefer the interstitial sites in bcc metals due to their small size compared to the matrix atoms. The solution energies of C atoms at the T- and O-sites are 1.54 and 0.70 eV/atom, respectively. The solution energy difference between these two sites is 0.84 eV, which meets the DFT calculations of ~ 1.0[61] and 0.86 eV.[62] The diffusion path of C atoms in α-Fe is between neighboring O-sties with an energy barrier of 0.84 eV, also in line with the DFT results of 0.86 eV,[61] 0.87 eV.[62] The solution energy of carbon in α-Fe shows a similar response to volumetric strain as that of the H atoms (see Fig. 3a). However, the diffusion energy barriers (ΔE) show contrasting behavior. ΔE increased from 0.78 eV at $\varepsilon = -5.88\%$ to 0.86 eV at $\varepsilon = 6.12\%$. Within the considered volumetric strains, the solution energies and diffusion barriers are in line with own DFT results.

Figure 3b shows the trapping energies of various numbers of C atoms in a monovacancy, which were obtained using the same model and method employed in the H-vacancy system (see Sect. NNIP Performance for α-Iron with Hydrogen). Additional own DFT results are also presented in the figure, and a good agreement between NNIP and DFT can be observed. The configurations of 2 and 4 C atoms in vacancies are different from those for the H case (see Fig. 2b). A monovacancy energetically prefers trapping 2 C atoms and is capable of accommodating up to 3 C atoms at 0 K. The local atomic configurations and energy barriers of the diffusion of a C-vacancy complex in α-Fe predicted by the NNIP are shown in Fig. 3c. The diffusion path was taken from a prior DFT study.[63] The NNIP successfully captured all the relevant details of the diffusion event. Figure 3d presents the carbon solution energy and its effect on the $\Sigma5(310)[001]$ GB formation

energy. Employing the same GB model in Sect. NNIP Performance for α-Iron with Hydrogen, up to 4 C atoms were gradually introduced to the GB region following the same sequence as that of H (see Fig. 2d). The formation energy of GB decreased from 1.59 to 0.45 J/m^2 as the number of C atoms at GB increased from 0 to 4. The formation energy reduction is more significant than that of the H-segregation case, which quantitatively agrees with the DFT results,[59,64] as shown in the upper panel of Fig. 3d. The solution energy is around -1.0 eV/atom when there is no more than 2 C atoms segregated at the GB, and it rapidly increases to -0.45 eV/atom when more than 2 C atoms segregated to the GB (lower panel of Fig. 3d). This result is nicely in line with that from the DFT calculations.[64] Mechanical and chemical components of the solution energy can be found in the Supplementary Materials (see Table S3).

Cementite (Fe$_3$C) is the most commonly observed iron carbide in steel,[66] thus it is essential to ensure NNIP can work well for this system. The lattice constants and elastic constants predicted by the NNIP, along with available results from FeC-NNIP,[40] DFT,[67,68] and experiments,[69] are summarized in Table I. A good agreement is observed between these results.

The phonon dispersion curves along the high symmetry path was shown in Fig. 3c, which is in line with the reported DFT results.[67] The formation energy of various points defects in Fe$_3$C are predicted using a supercell with 128 atoms. For the formation energy definition and the reference system, refer to the DFT work.[65] The vacancy formation energy of C atom of 0.5 eV is lower than that of Fe atom (1.5–2.0 eV). The antisite formation energies for all three cases have no significant differences (around 3.0 eV), while the interstitial of C atom is much lower than that of Fe atom, (C: 0.75 eV, Fe: 5.3 eV). As displayed in Fig. 3d, the NNIP results quantitatively agree with those obtained using DFT calculations.[65]

It is known that the C atoms can stabilize the hard core configuration of screw dislocation of BCC metals,[70–72] but it is difficult for EIPs to correctly describe this phenomenon.[8,70,73] To present the performance of the NNIP in this scenario, a C atom was initially set at an O-site near the core of screw dislocation (length = $2b$). The system spontaneously reorganized and relaxed towards a hard core configuration with the C atom at the center upon the structural relaxation, as illustrated in the left panel of Fig. 4a. The structural parameters of the C atom-decorated screw dislocation are presented in the right panel of Fig. 4a, and quantitatively match the DFT results.[70]

The interaction energy of the C atom with the reconstructed screw dislocation has been studied following the same manner as the DFT work.[70] The carbon-dislocation interaction energy was -0.55 eV when a C atom was introduced to a model with the
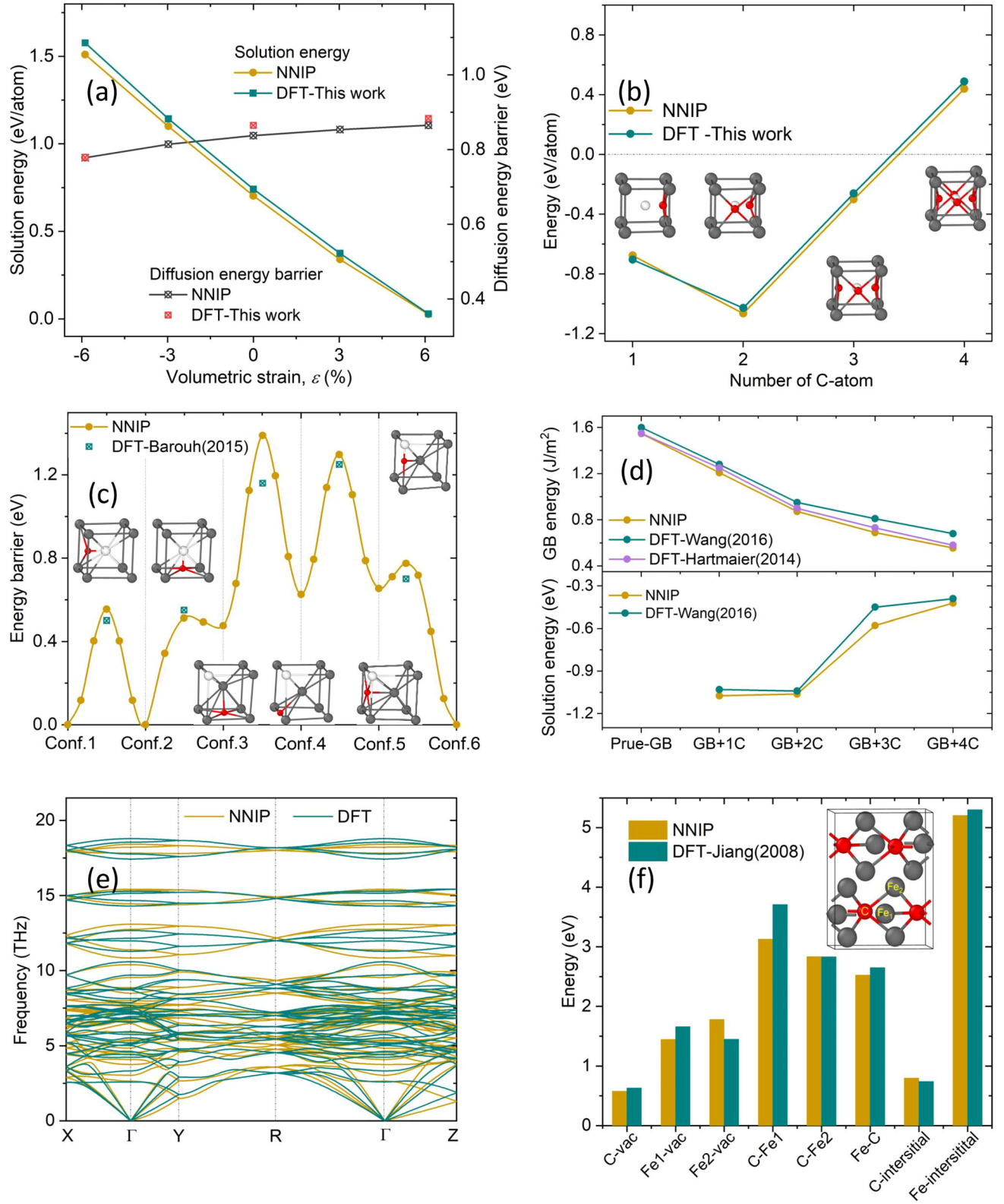
A Neural Network Interatomic Potential for the Ternary α-Fe-C-H System: Toward Million-Atom Simulations of Hydrogen Embrittlement in Steel

Fig. 3. NNIP performance for α-iron with carbon, and carbide(Fe_3C): (a) volumetric strain effects on solubility and diffusivity of C atom in pure α-iron, (b) local atomic configuration and trapping energy of various number of C atoms in monovacancy; the white balls stand for the vacancy. (c) Energy profile and local atomic configurations of the diffusion of a vacancy-C complex. (d) C solution energy (*lower panel*) and its effects on formation energy (*upper panel*) of a symmetric tilt Σ5(310)[001] GB. The site of C at GB sheared the same setting as that for H case; see Fig. 2d. (e) Phonon dispersion curves for Fe_3C. (f) Formation energy of various point defects in Fe_3C. The available reported DFT results[65] are also plotted.

Table I. Lattice constant and elastic constants of cementite obtained by NNIPs, DFT calculations, and experimental

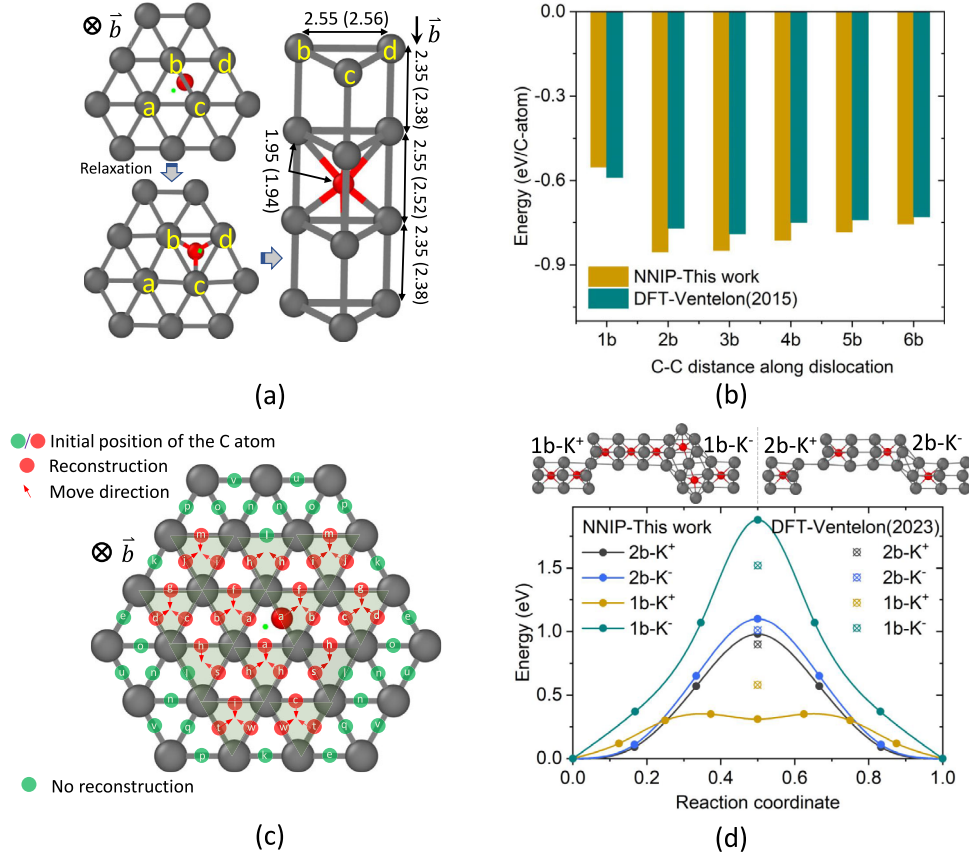| Method	Lattice constants, Å			Elastic constants, GPa								
	a	b	c	C_{11}	C_{22}	C_{33}	C_{12}	C_{13}	C_{23}	C_{44}	C_{55}	C_{66}
NNIP	5.018	6.757	4.462	371	358	333	185	155	202	15	131	116
FeC-NNIP[40]	5.020	6.737	4.469	365	341	310	172	153	177	14	122	115
DFT[67]	5.04	6.72	4.48	388	345	322	156	164	162	15	134	134
DFT[68]	5.036	6.724	4.480	385	341	316	157	162	167	13	131	131
Exp[69]	5.08	6.73	4.51	–	–	–	–	–	–	–	–	–

Fig. 4. NNIP performance for the interaction of screw dislocation with C atoms: (a) dislocation core reconstruction introduced by C atoms; the structural parameters obtained from the NNIP are shown, with the corresponding DFT values shown in parentheses. (b) Interaction energy of screw dislocation and C atom (l_{C-C} = (1-6)b). (c) A carbon atom was set at various O-site (red- or green-filled circles) near the easy core of screw dislocation. The arrows indicate the position of the C atom after the structure relaxation. The shaded triangles indicate the hard-core region centered on the C atom. Red- and green-filled circles represent whether reconstruction occurs or does not occur, respectively. The green point indicates the dislocation line obtained by the DXA tool implemented in the OVITO code;[75] the length of the dislocation in model is 2b. (d) The atomic configurations of C decorated kink-pairs with l_{C-C} = 1b and 2b are displayed in the *upper panel.*, and the Energy variations during the migration of the kinks with different C separations are shown in the *lower panel*, along with available DFT results.[76] $\vec{b}$ in (a) and (c) stands for the Burgers vector direction and its length is b (Color figure online).

dislocation length of 1b (i.e., C-C separation is 1b along the dislocation line, l_{C-C} = 1b), very close to that of the DFT results of −0.59 eV.[70] Upon increasing the separation between neighboring C atoms, the interaction energy first decreases rapidly to −0.85 eV for l_{C-C} = 2b, and then increases gradually to −0.75 eV for l_{C-C} = 6b. The above-mentioned interaction energy is presented in

Fig. 4b, and the corresponding reported DFT results[70] are also plotted. The neighboring C atoms with a separation of 2b is the most energetically preferred configuration.

Whether or not the aforementioned reconstruction occurs for various relative positions of the C atom to the screw dislocation has been studied by using DFT calculations,[74] which supplies the

reliable benchmark for the test of the transferability of NNIP in this scenario. The results are summarized in Fig. 4c. The red-/green-filled circles stand for the initial position of the C atom. The red arrow for each red-filled circle indicates the motion direction of the C atom during the structure relaxation. The tip of the arrow roughly shows the relaxed position of the C atom and is also the center of the reconstructed hard core. No arrows were assigned for the green-filled circles because the reconstruction did not occur during relaxation. Finally, all the red circles are surrounded by green circles and the capture radius, r_{cap}, of dislocation to the C atom, can be estimated. We can conclude that the r_{cap} predicted by this NNIP is less that $2d$ (d is the distance between neighboring Peierls valleys, $d = a_0 \times \sqrt{2/3}$). An exception is that the structure is stable when the C atom is at the site, l (and the other two equivalent sites, see Fig. 4c); this is also presented in the DFT prediction.[74]

The atomic configuration of the C-decorated screw dislocation, along with the energy barriers for kink migration, has been reported based on DFT calculations.[76] The dislocation dipole model (Fig. 2e) was employed, incorporating a dislocation length of $8b$ and $l_{C-C} = 1b$ and $2b$ to evaluate the transferability of the NNIP in describing C-decorated dislocation. Two nonequivalent kinks, denoted as K$^+$ and K$^-$, were formed on the C-decorated screw dislocation, as illustrated in the upper panel of Fig. 4d. These configurations are consistent with those predicted by the Fe-C NNIP[40] and are similar as those obtained from DFT calculations.[76] A dipole model with a dislocation length of $40b$ and kinks distance of $20b$ was employed to determine the migration energy barriers of four types of kinks (1b-K$^\pm$, 2b-K$^\pm$). The migration energy barriers predicted by the NNIP for 1b-K$^+$ and 1b-K$^-$ kinks are 0.35 and 1.88 eV, respectively, while those for 2b-K$^+$ and 2b-K$^-$ are 0.98 eV and 1.10 eV, respectively. In comparison with the DFT results (0.58 eV, 1.52 eV, 0.92 eV, and 1.01 eV for the four energy barriers[76]), the NNIP predictions exhibit deviations that remain within an acceptable range.

It is not surprising that the NNIP reached the same accuracy as the NNIP for α-Fe-C binary system reported in our previous work,[40] because the database used for the training of the α-Fe-C NNIP was totally included from the current database.

NNIP Performance for α-Iron, Carbon, and Hydrogen Ternary System

To check the performance of the NNIP for the ternary system, C and H co-trapping in vacancies, co-segregation at GB, H solubility and diffusivity in Fe$_3$C, and H solubility at the ferrite–cementite interface were considered.

For co-trapping in vacancies, an H atom was introduced to the C-trapped vacancy configuration (see Fig. 5a). The trapping energy of the H atom in a vacancy with 1 trapped C atom is − 0.56 eV/atom, agreeing well with the reported DFT result of 0.6 eV/atom.[77] The trapping energies of the second, third, and fourth H atoms have a similar trapping energy of − 0.16 eV/atom. Both NNIP and DFT calculations obtained up to 4 H can be accommodated for a 1 C pre-trapped vacancy. For the vacancy with 2 pre-trapped C atoms, up to 3 H atoms could be trapped but the final two with a trapping energy close to 0 eV. A vacancy pre-trapped with 3 C atoms cannot accommodate additional H atoms, even though the 3C-2H configuration shows negative trapping energy. In this configuration, the hydrogen atoms are not located within the vacancy but at two adjacent T sites. The configurations and trapping energies (of the last H atoms) of all combinations of the C and H in vacancies predicted by NNIP and DFT are shown in Fig. 5a.

Following the same manner as the co-trapping in vacancies, the property of C and H co-segregation at GB was further checked, and the results are summarized in Fig. 5b. The GB formation energy gradually decreased as increasing the C or H atoms segregated at the GB. The GB formation energy was 1.075 J/m^2 when two H atoms and one C atom were at GB, which perfectly meets the DFT results of 1.08 J/m^2[59] (not shown in the upper penal of Fig. 5b). For other combinations of the impurities of nC+mH ($m+n \leq 4$) segregated at the GB, the GB formation energy and the segregation energy of the final H atoms are systematically predicted using NNIP and confirmed by additional DFT calculations (see Fig. 5b), and a good agreement between NNIP and DFT is presented. Note that various numbers of H and/or C atoms in the GBs were set, and that DFT-based MD calculations were performed to sample the interaction between the H, C and Fe atoms.

There are four independent solution sites of H atoms in Fe$_3$C (i.e., $s1$–$s4$, see Fig. 5c; $s5$ is an equivalent site of $s1$). The energetically preferred solution site is a O-like site of $s1$, with a solution energy of −0.02 eV, which fairly well agrees with own DFT result of 0.02 eV. Solution energies of H atoms occupying $s2$, $s3$, and $s4$ are 0.688, 0.522, and 0.760 eV, respectively, and all of them show good agreement with our own DFT results of 0.726, 0.568, and 0.800 eV, respectively. Comparing with the solution energy of H atom at a T-site in α-Fe (0.22 eV), $s1$ is more energetically preferred than any other sites. All of these data are included in the database.

The diffusion energy barrier for an H atom diffusion along a path between the neighboring equivalent $s1$ ($s1 \rightarrow s2 \rightarrow s3 \rightarrow s5$, see Fig. 5c) has been predicted by NNIP and is shown in Fig. 5d. The diffusion barrier is about 0.8 eV, which is much larger than that of the H atom diffusion in α-Fe (0.09 eV), indicating that H atoms can be deeply
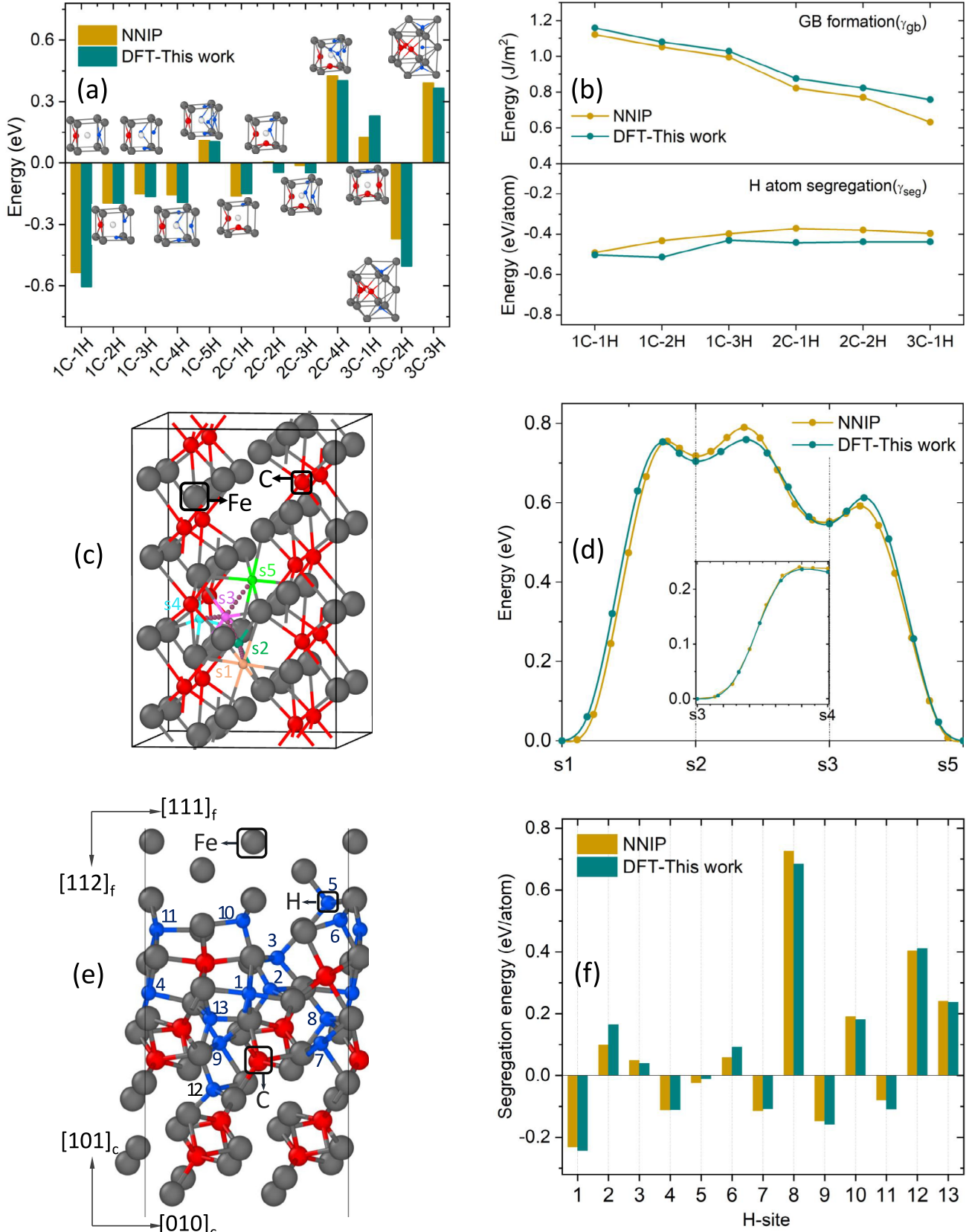
Fig. 5. The NNIP performance for the α-Fe-C-H system: (a) C-H co-trapping in a monovacancy, (b) C-H co-segregation at a symmetric tilt GB, (c) and (d) H solution sites and diffusivity in Fe_3C, (e) and (f) H trapping sites and the corresponding trapping energies at a ferrite–cementite interface; our own DFT results are also plotted.

trapped in cementite. One more diffusion branch of $s3 \rightarrow s4$ was also tested. Both the total diffusion barrier and the value of each hump in diffusion paths are in line with reported DFT results[66,78] and our own DFT calculations. The behavior of H atoms in Fe_3C bulk is well captured. Note that this property is not explicitly trained.

The interface between ferrite and nanoprecipitates in martensitic steels has attracted great interest, and the hydrogen trapping and exclusion at the interface play a critical role in the understanding of the HE phenomenon.[79–81] However, an accurate atomistic description of hydrogen behavior at cementite–ferrite boundaries is still challenging.[66] Thus, the H segregation energy at and around the ferrite–cementite interface have been examined. The H segregation energies were determined by taking the H solution energy at a T-site within the grains as the reference, and the results are shown in Fig. 5e and f. The results from the NNIP are well in line with those from DFT calculations. Each H-trapped interface model from NNIP was further reinforced by DFT calculations, and the results show that there is no significant change in energy (also in the structure, but not shown), which means that the NNIP can well describe the ground state of this H-soluted interface system.

RESULTS: LARGE-SCALE TENSILE SIMULATION OF THE FE-C-H TERNARY SYSTEM

To demonstrate the effectiveness of the developed NNIP and its feasibility for large-scale atomic simulations, we performed a tensile simulation using a 1-million-atom Fe-C-H model. The model, sized at $80a_0 \times 80a_0 \times 80a_0$, was initially constructed with orientations of x[100], y[010], and z[001], containing 1,024,000 Fe atoms. Information on the computational cost of this simulation is presented in the Supplementary Materials (see Note 2).

Before beginning the tensile simulation, we introduced dislocations, vacancies, and other defects through a pre-compression procedure along the z-direction. As part of this procedure, we first inserted 256 randomly distributed vacancy–interstitial pairs to serve as seeds for dislocation nucleation. The model was compressed by approximately 20% along the z-direction, while the dimensions in the other two directions were adjusted to preserve a constant volume. Afterward, an MD simulation was conducted under the NVT ensemble at 900 K for 100 ps to generate defects. Note that, for computational efficiency during this pre-processing stage, we employed an EAM potential.[4]

All subsequent simulations were performed using the NNIP developed in this work. After the pre-compression, the model was annealed at 300 K in 1 ps under the NPT ensemble to create the reference Model-I (pure α-Fe). Next, 0.2 at.% (4096) C

atoms were introduced randomly into the same model to construct Model-II (α-Fe-C). Subsequently, an additional 1 at.% (10,240) H atoms were randomly introduced to construct Model-III (α-Fe-C-H). To equilibrate the distribution of C and/or H atoms, we carried out a 25-ps MD annealing simulation at 300 K under the NPT ensemble. We confirmed that all the models maintained nearly identical dislocation densities and vacancy concentrations after annealing. The constructed models are shown in Fig. 6a, b, and c.

Uniaxial tensile tests were then performed on these models. A constant engineering strain rate of $2 \times 10^8 \, s^{-1}$ was applied along the z-direction, while zero-pressure conditions were imposed along the x- and y-directions. The tensile simulations were carried out at 300 K with a time step of 0.5 fs.

In these models, the dislocation network is predominantly composed of dislocations with a Burgers vector of $\frac{1}{2}\langle111\rangle$, with a smaller proportion of $\langle100\rangle$ dislocations. The dislocation density is approximately $1 \times 10^{17} \, m^{-2}$, which is considerably high due to the severe plastic deformation introduced during the model preparation process.

In Model-II, a small number of C atoms remained trapped in vacancies and along dislocations, even after a 25-ps MD simulation, because of their initially random distribution and the low diffusivity at the simulation temperature. In actual materials, however, sufficient annealing typically takes place, and, as noted above, an attractive interaction exists between dislocations (or vacancies) and the C atoms. Consequently, dislocations and vacancies would be more strongly bound to C under experimental conditions. This discrepancy implies that, strictly speaking, the stress required to initiate dislocation motion in our simulation may differ from that in experiments. Nonetheless, once plastic deformation begins, the very limited diffusion of C at room temperature over experimental timescales suggests that, if the strain rates were comparable, one could still analyze the stress contributions from dislocation–C interactions in a manner consistent with experimental observations. It is important to note, however, that the strain rates in MD simulations are extremely high compared to experiments. These high strain rates can dramatically increase dislocation velocities, amplify defect-generation rates, and overshoot the stress required for dislocation motion, making fully quantitative comparisons challenging.

Model-III exhibited a similar carbon distribution, while a greater number of hydrogen atoms were trapped at defects, reflecting the high diffusivity of H. Because the strain rates in MD simulations are so high, the amount of hydrogen that can be trapped by moving dislocations is likely reduced, potentially leading to an underestimation of the drag effect of hydrogen on dislocation mobility. This possibility must be kept in mind when interpreting the simulation results.
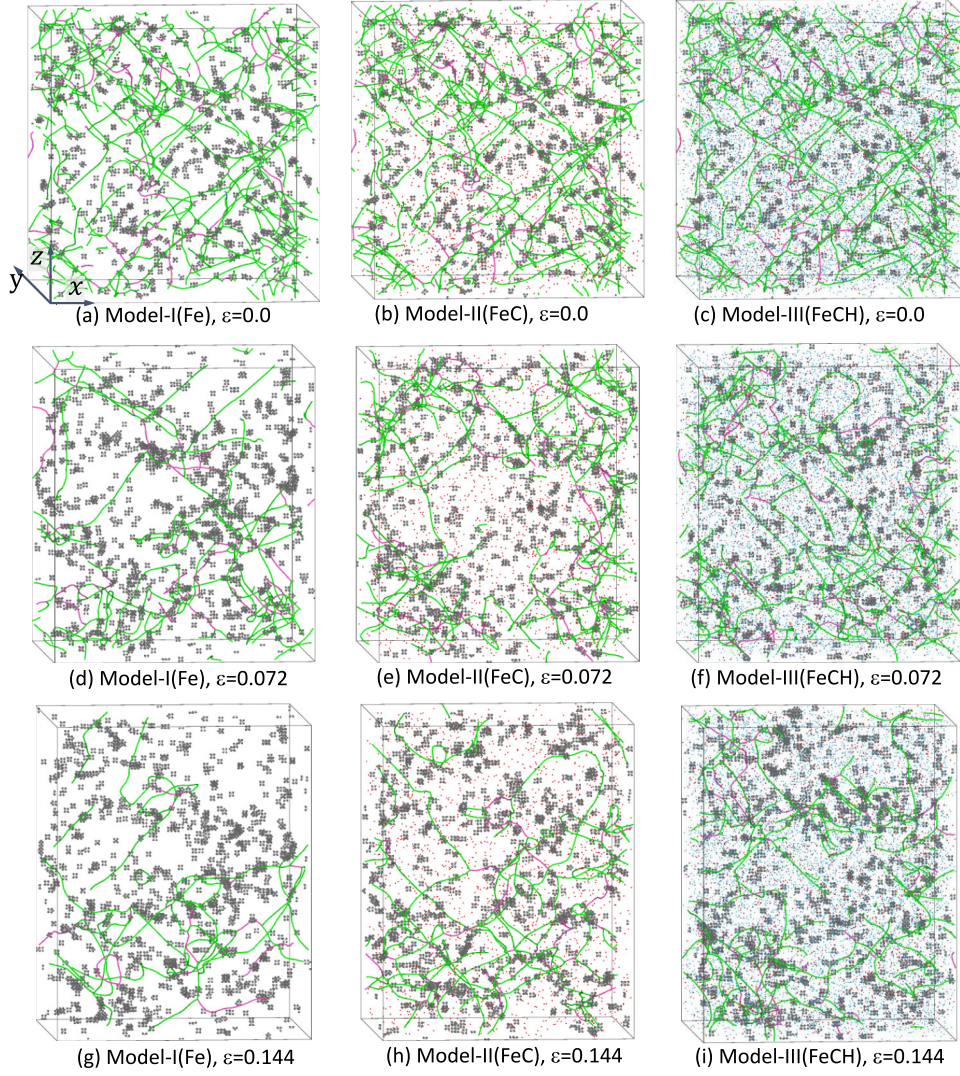
Fig. 6. Defective models used for the tensile tests: (a), (d), (g) model with dislocations and point defects (Model-I). (b), (e), (h) model with dislocations, point defects, and C atoms (Model-II). (c), (f), (I) model with dislocations, point defects, and C and H atoms (Model-III). The strain (ε) of each snapshot was also provided. The green and red lines represent dislocations with Burgers vectors of $12\langle 111 \rangle$ and $\langle 100 \rangle$, respectively, identified using the DXA[75] tool implemented in the OVITO package.[32] The gray, red, and blue spheres correspond to Fe, C, and H atoms, respectively. Only the Fe atoms around vacancies are shown (Color figure online).

Results of the uniaxial tensile MD simulations conducted after the pre-compression step are shown in Fig. 6d–i, illustrating time-dependent configurations of dislocations, vacancies (and vacancy clusters), as well as C and H atoms. Corresponding movies are provided as Supplementary Materials (see Movies S1–S3). The stress–strain relationship is shown in Fig. 7a, the evolution of dislocation density in Fig. 7b, and the number of vacancies (including those within vacancy clusters) in Fig. 7c.

All models exhibit a decrease in the dislocation density introduced by pre-compression when subjected to uniaxial tension, confirming that mechanical annealing is in progress. In each model, this mechanical annealing becomes prominent around an engineering strain of 0.01–0.02, corresponding to the onset of activity of the pre-introduced dislocations. Model-I shows the lowest stress required to

initiate dislocation motion, followed by Model-II and then Model-III. This behavior arises from the presence of C near dislocations and H trapped at dislocations, both of which impede dislocation activation.

As the strain increases further, dislocation activity in Model-I becomes especially noticeable, leading to pronounced mechanical annealing and a significant reduction in dislocation density. In contrast, dislocation activity in Model-II and Model-III is more limited, resulting in a slower reduction in dislocation density. Between these two, dislocation activity is even more constrained in Model-III, partly because C and H can interact with moving dislocations and hinder their motion. Figure 8a illustrates how C atoms impede dislocation motion. However, we propose an additional mechanism: as plastic deformation proceeds, vacancies,
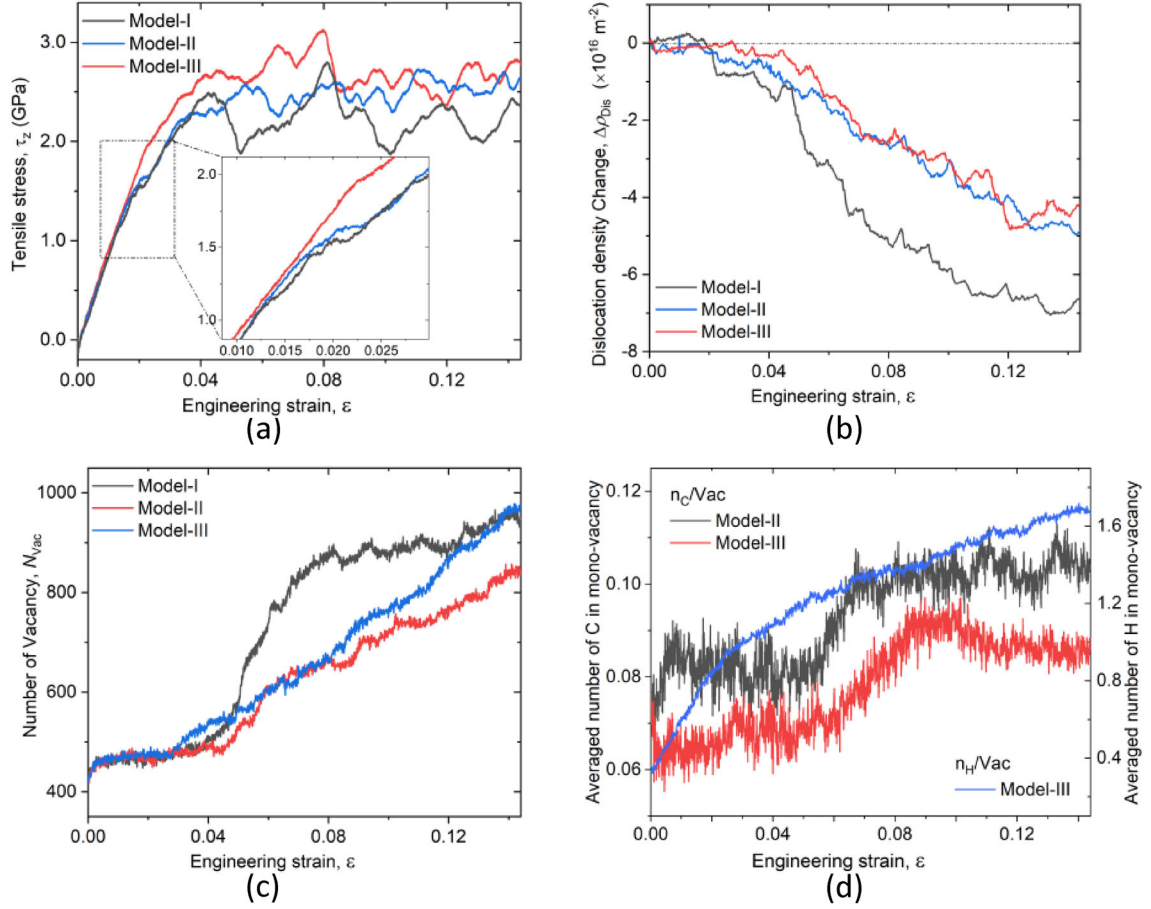
Fig. 7. Results of the simulations: (a) strain–stress curve in the tensile tests for the three models; (b) the change of dislocation densities in the three models as a function of tensile strain; (c) number of vacancies in models in the whole tensile tests; (d) average number of C and H atoms per vacancy for Model-II and Model-III in the tensile test.
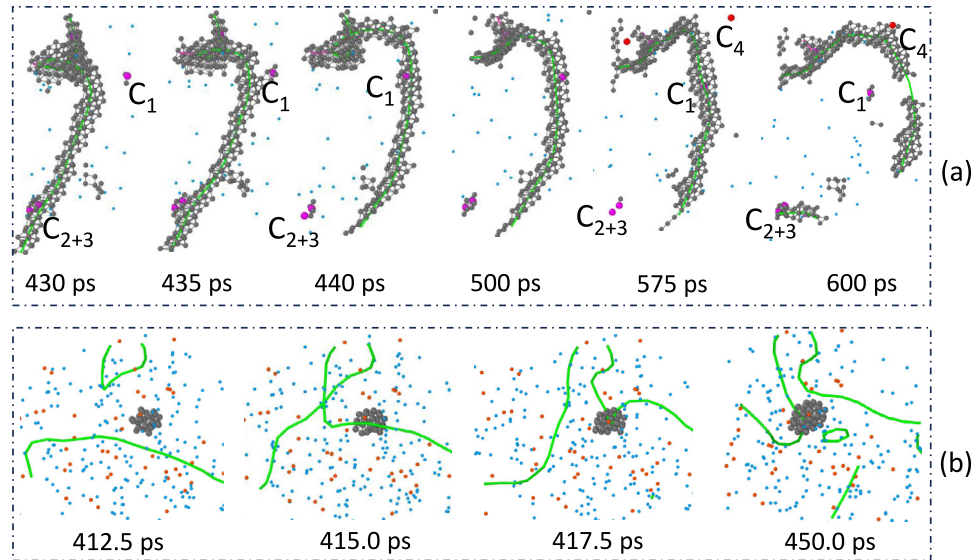

Fig. 8. Defects drag effects on the motion of dislocation: (a) interaction of C (H) atoms with a traveling dislocation, and hinder its motion; (b) interaction of vacancies cluster with moving dislocations, which could enhance the growth of vacancy cluster. The cluster size, defined as the number of Fe atoms comprising the vacancy cluster, increased from 29 to 40 as the result of its interaction with a passing dislocation. Blue and red dots represent H and C atoms, respectively, while gray spheres denote Fe atoms. Only the Fe atoms associated with the dislocation in (a) and the vacancy cluster in (b) are shown. The green lines stand for the dislocations and obtained by OVITO (Color figure online).[32]

interstitials, and vacancy clusters generated through mutual interactions between dislocations or between dislocations and defects (vacancies, interstitials, vacancy clusters, C, H, and so on) can further interact with dislocations, inhibiting their subsequent motion (see Fig. 8b).

Beyond a strain of 0.04, all the models exhibit a nearly constant flow stress. Comparing the flow stress of Model-II and Model-III beyond a strain of 0.04 shows that Model-III's flow stress is slightly higher. In addition to the drag effect exerted by H on dislocations, this difference stems from the influence of lattice defects on dislocation motion, as discussed above. Figure 7c presents the evolution of the number of vacancies (N_{Vac}) during uniaxial tension. It is evident that Model-III generates a larger number of vacancies than Model-II, which elevates the required stress by restricting dislocation motion.

Comparing Model-I and Model-II reveals that, although Model-II shows a slightly higher flow stress, both models exhibit quite similar flow stresses despite the absence of C or H in Model-I. One likely explanation is that mechanical annealing in Model-I proceeds more extensively than in Model-II beyond a strain of 0.04, leading to a substantial reduction in the dislocation density responsible for plastic deformation (Fig. 7b). Moreover, lattice defects such as vacancies and vacancy clusters generated during this process (Fig. 8a) hinder dislocation motion, thereby increasing the resistance to plastic deformation.

The formation of vacancies and vacancy clusters in these models can promote the generation of additional vacancies and vacancy clusters through interactions with subsequent dislocations (Fig. 8b). However, the creation of vacancies and vacancy clusters is also accompanied by the formation of interstitials. Because interstitials can diffuse rapidly even at room temperature,[82] many of them recombine with vacancies or vacancy clusters, thus eliminating these defects (although some interstitials may escape to GBs or surfaces). While the high strain rates in MD simulations limit such recombination, it is plausible that, under experimental strain rates for pure α-Fe, many vacancies and vacancy clusters would be removed via recombination.

When C or H is present, however, an attractive interaction exists between these solutes and vacancies, as shown in the previous section. By forming complexes with vacancies, C and H stabilize these vacancies. Figure 7d illustrates the time evolution of the number of C and H atoms trapped by vacancies, demonstrating that such complexes form. Consequently, the annihilation of vacancies via recombination with interstitials is inhibited, potentially accelerating the generation of vacancies and the growth of vacancy clusters, which may ultimately lead to accelerated material failure.

Figure 7c compares the number of vacancies and vacancy clusters in each model. However, direct comparison of these raw numbers among the models is not entirely fair because their plastic strain rates differ. Therefore, at each strain (or time), we normalize the vacancy generation rate $\dot{N}_{Vac}$ by the equivalent plastic strain rate $\dot{\varepsilon}_{eq}$, defining the normalized vacancy generation rate $\dot{n}_{Vac}$:

$$\dot{n}_{Vac} = \frac{\dot{N}_{Vac}}{\dot{\varepsilon}_{eq}}. \tag{5}$$

where:

$$\dot{\varepsilon}_{eq} = \sqrt{\frac{2}{3}\,\dot{\varepsilon}_{ij}^{p}\,\dot{\varepsilon}_{ij}^{p}}, \tag{6}$$

$$\dot{\varepsilon}_{ij}^{p} = \dot{\varepsilon}_{ij}^{tot} - \dot{\varepsilon}_{ij}^{e}, \tag{7}$$

$$\dot{\varepsilon}_{ij}^{e} = S_{ijkl}\,\dot{\sigma}_{kl}. \tag{8}$$

where $\dot{\varepsilon}_{ij}^{p}$, $\dot{\varepsilon}_{ij}^{tot}$, and $\dot{\varepsilon}_{ij}^{e}$ are the plastic, total, and elastic (true) strain-rate tensors, respectively. The total strain-rate tensor is directly obtained from the deformation of the simulation cell. The elastic strain-rate tensor is calculated from the true stress σ_{ij} acting on the simulation cell using the elastic compliance tensor S_{ijkl} computed by NNIP elastic stiffness for pure α-iron, assuming S_{ijkl} does not change during deformation. (Strictly speaking, because defects accumulate during plastic deformation, the elastic compliance would be expected to increase slightly.) Moreover, the variations in $\dot{\varepsilon}_{eq}, \dot{\varepsilon}_{ij}^{e}, \dot{\varepsilon}_{ij}^{p}$ are shown in Supplementary Materials (see Fig. S5).

We averaged the data for $\dot{n}_{Vac}$ from strain 0.05, where plastic deformation becomes significant, to strain 0.14. The resulting values are shown in Fig. 9. Among the three models, Model-I exhibits the smallest normalized vacancy generation rate, followed by Model-II and Model-III in ascending order. Note that this rate implicitly accounts for vacancy–interstitial recombination, which annihilates vacancies. These findings show that adding C or H promotes the formation of lattice defects, such as vacancies and vacancy clusters, during plastic deformation, and that H tends to amplify this effect. The proliferation of vacancies and vacancy clusters further increases the likelihood of collisions between dislocations and these defects, leading to the formation of even more vacancies and larger vacancy clusters. Considering H's enhancing effect, it follows that the presence of H can accelerate material damage associated with plastic deformation.

A Neural Network Interatomic Potential for the Ternary α-Fe-C-H System: Toward Million-Atom Simulations of Hydrogen Embrittlement in Steel
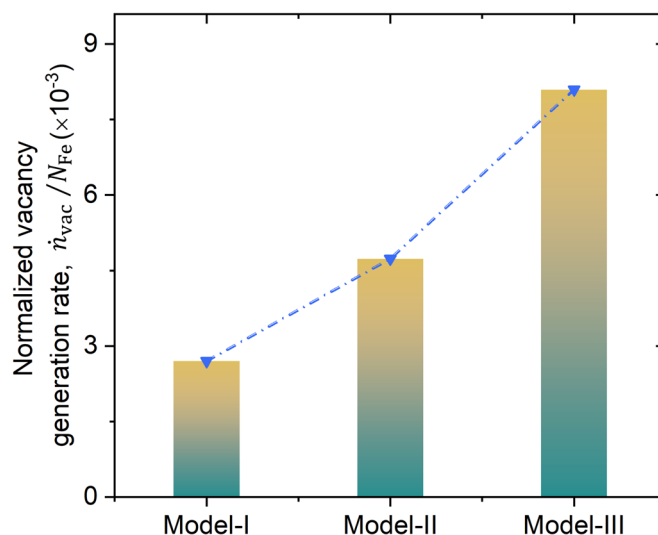

Fig. 9. Normalized vacancy generation rate of the three models. N_{Fe} is the number of iron atoms in the model.

CONCLUSION

A high accuracy neural network interatomic potential for the Fe-C-H system was constructed based on a comprehensive reference database obtained by extensive DFT calculations. In the validation part, we systematically tested the NNIP performance for the systems of pure α-iron, interaction of hydrogen with defective α-iron, and interaction of carbon with defective α-iron, as well as basic properties of the cementite, ferrite–cementite interface, interaction of C and H atoms with defective α-iron, and interaction of H with cementite and its interface with ferrite. The test results provide us with evidence of the good transferability and reliability of the current NNIP, such as the prediction of the screw dislocation core configuration reconstruction induced by C or H atoms, which is difficult for EIPs.

Using our newly developed neural network interatomic potential, we performed MD tensile simulations on a one-million-atom model, and found that both C and H impede dislocation mobility, and that newly formed vacancies (and vacancy clusters) during plastic deformation likewise hamper dislocation motion. The vacancy generation rate is accelerated by C and H, as these solute-dislocation interactions and the formation of vacancy–C/H complexes inhibit vacancy–interstitial recombination, ultimately promoting further vacancy accumulation and intensifying material damage. Although the strain rates in our simulations are much higher than those typically employed in experiments, these findings provide key insights into the fundamental role of solute atoms in defect-mediated plasticity, and validate the feasibility of the developed NNIP for large-scale simulations.

AUTHOR CONTRIBUTIONS

S.O. designed the research, F.-S.M. constructed and tested the neural network interatomic potential, F.-S.M, K.M., J.-P.D. and P.-J. Y. performed DFT calculations, and F.-S.M, S.S. conducted the MD simulations. F.-S.M. and S.O. drafted the manuscript. All authors analyzed and interpreted the data and edited the final submission.

DATA AVAILABILITY

The constructed neural network interatomic potential in this study has been shared online: https://github.com/mengfsou/NNIP-FeCH. The database is available upon reasonable request to the corresponding author. A neuroevolution potential (NEP), based on the same database, is also available in the GitHub repository referenced above.

CONFLICT OF INTEREST

The authors declare that they have no conflict of interest.

OPEN ACCESS

REFERENCES

1. M. Mendelev, et al., *Phil. Mag.* 83, 3977–3994 https://doi.org/10.1080/14786430310001613264 (2003).
2. G. Ackland, M. Mendelev, D. Srolovitz, S. Han, and A. Barashev, *J. Phys.: Condens. Matter* 16, S2629 https://doi.org/10.1088/0953-8984/16/27/003 (2004).
3. A. Ramasubramaniam, M. Itakura, and E.A. Carter, *Phys. Rev. B* 79, 174101 https://doi.org/10.1103/PhysRevB.79.174101 (2009).
4. M. Wen, *Comput. Mater. Sci.* 197, 110640 https://doi.org/10.1016/j.commatsci.2021.110640 (2021).
5. C. Becquart, et al., *Comput. Mater. Sci.* 40, 119 https://doi.org/10.1016/j.commatsci.2006.11.003 (2007).
6. K. Hyodo, S. Munetoh, and T. Tsuchiyama, *Comput. Mater. Sci.* 184, 109871 https://doi.org/10.1016/j.commatsci.2020.109871 (2020).
7. K. Ito, Y. Tanaka, K. Tsutsui, and H. Sawada, *Comput. Mater. Sci.* 225, 112196 https://doi.org/10.1016/j.commatsci.2023.112196 (2023).
8. A. Allera, F. Ribeiro, M. Perez, and D. Rodney, *Phys. Rev. Mater.* 6, 013608 https://doi.org/10.1103/PhysRevMaterials.6.013608 (2022).
9. O.A. Restrepo, et al., *Comput. Mater. Sci.* 112, 96 https://doi.org/10.1016/j.commatsci.2015.10.017 (2016).
10. X. Zhou, M.E. Foster, J.A. Ronevich, and C.W. San Marchi, *J. Comput. Chem.* 41, 1299 https://doi.org/10.1002/jcc.26176 (2020).
11. C. Nowak, R. Sills, J. Ronevich, C. San Marchi, and X. Zhou, *Int. J. Hydrog. Energy* 47, 32732 https://doi.org/10.1016/j.ijhydene.2022.07.166 (2022).
12. S. Mun, *et al. arXiv preprint* (2021). https://doi.org/10.48550/arXiv.2109.01712.
13. B.-J. Lee, *Acta Mater.* 54, 701 https://doi.org/10.1016/j.actamat.2005.09.034 (2006).
14. B.-J. Lee and J.-W. Jang, *Acta Mater.* 55, 6779 https://doi.org/10.1016/j.actamat.2007.08.041 (2007).
15. S. Mun, et al., *J. Phys. Chem. A* 121, 1502 https://doi.org/10.1021/acs.jpca.6b11343 (2017).
16. C. Zou, A.C. Van Duin, and D.C. Sorescu, *Top. Catal.* 55, 391 https://doi.org/10.1007/s11244-012-9796-0 (2012).
17. M.M. Islam, C. Zou, A.C. Van Duin, and S. Raman, *Phys. Chem. Chem. Phys.* 18, 761 https://doi.org/10.1039/C5CP06108C (2016).
18. E. Hayward and C.-C. Fu, *Phys. Rev. B* 87, 174103 https://doi.org/10.1103/PhysRevB.87.174103 (2013).
19. J. Behler and M. Parrinello, *Phys. Rev. Lett.* 98, 146401 https://doi.org/10.1103/PhysRevLett.98.146401 (2007).
20. A.P. Bartók, M.C. Payne, R. Kondor, and G. Csányi, *Phys. Rev. Lett.* 104, 136403 https://doi.org/10.1103/PhysRevLett.104.136403 (2010).
21. H. Tang, et al., *Acta Materialia* 238, 118217 https://doi.org/10.1016/j.actamat.2022.118217 (2022).
22. Y. Wang, et al., *Nat. Mater.* 20, 1371 https://doi.org/10.1038/s41563-021-01017-z (2021).
23. Z. Fan and H. Tanaka, *Nat. Commun.* 15, 368 https://doi.org/10.1038/s41467-023-44332-6 (2024).
24. L. Zhang, G. Csányi, E. van der Giessen, and F. Maresca, *Acta Mater.* 270, 119788 https://doi.org/10.1016/j.actamat.2024.119788 (2024).
25. A. Singraber, T. Morawietz, J. Behler, and C. Dellago, *J. Chem. Theory Comput.* 15, 3075 https://doi.org/10.1021/acs.jctc.8b01092 (2019).
26. J. Behler, *J. Chem. Phys.* 134, 074106 https://doi.org/10.1063/1.3553717 (2011).
27. G. Imbalzano, et al., *J. Chem. Phys.* 148, 241730 https://doi.org/10.1063/1.5024611 (2018).
28. F.-S. Meng, et al., *Phys. Rev. Mater.* 5, 113606 https://doi.org/10.1103/PhysRevMaterials.5.113606 (2021).
29. G. Kresse and J. Furthmüller, *Phys. Rev. B* 54, 11169 https://doi.org/10.1103/PhysRevB.54.11169 (1996).
30. S. Plimpton, *J. Comput. Phys.* 117, 1 https://doi.org/10.1006/jcph.1995.1039 (1995).
31. A. Singraber, J. Behler, and C. Dellago, *J. Chem. Theory Comput.* 15, 1827 https://doi.org/10.1021/acs.jctc.8b00770 (2019).
32. A. Stukowski, *Modell. Simul. Mater. Sci. Eng.* 18, 015012 https://doi.org/10.1088/0965-0393/18/1/015012 (2009).
33. A. Togo and I. Tanaka, *Scripta Mater.* 108, 1 https://doi.org/10.1016/j.scriptamat.2015.07.021 (2015).
34. P. Hirel, *Comput. Phys. Commun.* 197, 212 https://doi.org/10.1016/j.cpc.2015.07.012 (2015).
35. G. Henkelman, B.P. Uberuaga, and H. Jónsson, *J. Chem. Phys.* 113, 9901 https://doi.org/10.1063/1.1329672 (2000).
36. J. Behler, *Int. J. Quantum Chem.* 115, 1032 https://doi.org/10.1002/qua.24890 (2015).
37. D. Marchand and W. Curtin, *Phys. Rev. Mater.* 6, 053803 https://doi.org/10.1103/PhysRevMaterials.6.053803 (2022).
38. Q.-J. Li, et al., *Cell Rep. Phys. Sci.* 2, 100359 https://doi.org/10.1016/j.xcrp.2021.100359 (2021).
39. N. Artrith and J. Behler, *Phys. Rev. B* 85, 045439 https://doi.org/10.1103/PhysRevB.85.045439 (2012).
40. F.-S. Meng, et al., *Acta Mater.* 281, 120408 https://doi.org/10.1016/j.actamat.2024.120408 (2024).
41. J. Beeler Jr. and R. Johnson, *Phys. Rev.* 156, 677 https://doi.org/10.1103/PhysRev.156.677 (1967).
42. D. Kandaskalov, C. Mijoule, and D. Connétable, *J. Nucl. Mater.* 441, 168 https://doi.org/10.1016/j.jnucmat.2013.05.030 (2013).
43. L. De Schepper, et al., *Phys. Rev. B* 27, 5257 https://doi.org/10.1103/PhysRevB.27.5257 (1983).
44. M.-C. Marinica, F. Willaime, and N. Mousseau, *Phys. Rev. B* 83, 094119 https://doi.org/10.1103/PhysRevB.83.094119 (2011).

A Neural Network Interatomic Potential for the Ternary α-Fe-C-H System: Toward Million-Atom Simulations of Hydrogen Embrittlement in Steel

45. C.-C. Fu, F. Willaime, and P. Ordejón, *Phys. Rev. Lett.* 92, 175503 https://doi.org/10.1103/PhysRevLett.92.175503 (2004).
46. D. Dragoni, T.D. Daff, G. Csányi, and N. Marzari, *Phys. Rev. Mater.* 2, 013808 https://doi.org/10.1103/PhysRevMaterials.2.013808 (2018).
47. H. Mori and T. Ozaki, *Phys. Rev. Mater.* 4, 040601 https://doi.org/10.1103/PhysRevMaterials.4.040601 (2020).
48. S. Klotz and M. Braden, *Phys. Rev. Lett.* 85, 3209 https://doi.org/10.1103/PhysRevLett.85.3209 (2000).
49. J. Wang, G.K. Madsen, and R. Drautz, *Modell. Simul. Mater. Sci. Eng.* 26, 025008 https://doi.org/10.1088/1361-651X/aa9f81 (2018).
50. D. Scheiber, R. Pippan, P. Puschnig, and L. Romaner, *Modell. Simul. Mater. Sci. Eng.* 24, 035013 https://doi.org/10.1088/0965-0393/24/3/035013 (2016).
51. S.K. Bhattacharya, S. Tanaka, Y. Shiihara, and M. Kohyama, *J. Mater. Sci.* 49, 3980 https://doi.org/10.1007/s10853-014-8038-1 (2014).
52. F. Maresca, D. Dragoni, G. Csányi, N. Marzari, and W.A. Curtin, *NPJ Comput. Mater.* 4, 1 https://doi.org/10.1038/s41524-018-0125-4 (2018).
53. M. Itakura, H. Kaburaki, M. Yamaguchi, and T. Okita, *Acta Mater.* 61, 6857 https://doi.org/10.1016/j.actamat.2013.07.064 (2013).
54. M. Wakeda, et al., *Acta Mater.* 131, 445 https://doi.org/10.1016/j.actamat.2017.04.017 (2017).
55. L. Dezerald, et al., *Phys. Rev. B* 89, 024104 https://doi.org/10.1103/PhysRevB.89.024104 (2014).
56. L. Proville, L. Ventelon, and D. Rodney, *Phys. Rev. B* 87, 144106 https://doi.org/10.1103/PhysRevB.87.144106 (2013).
57. L. Dezerald, L. Proville, L. Ventelon, F. Willaime, and D. Rodney, *Phys. Rev. B* 91, 094105 https://doi.org/10.1103/PhysRevB.91.094105 (2015).
58. Y. Tateyama and T. Ohno, *Phys. Rev. B* 67, 174105 https://doi.org/10.1103/PhysRevB.67.174105 (2003).
59. A. Tahir, R. Janisch, and A. Hartmaier, *Mater. Sci. Eng., A* 612, 462 https://doi.org/10.1016/j.msea.2014.06.071 (2014).
60. P.P. Borges, E. Clouet, and L. Ventelon, *Acta Mater.* 234, 118048 https://doi.org/10.1016/j.actamat.2022.118048 (2022).
61. D. Jiang and E.A. Carter, *Phys. Rev. B* 67, 214103 https://doi.org/10.1103/PhysRevB.67.214103 (2003).
62. M. Souissi, Y. Chen, M.H. Sluiter, and H. Numakura, *Comput. Mater. Sci.* 124, 249 https://doi.org/10.1016/j.commatsci.2016.07.037 (2016).
63. C. Barouh, T. Schuler, C.-C. Fu, and T. *Phys. Rev. B* 92, 104102 https://doi.org/10.1103/PhysRevB.92.104102 (2015).
64. J. Wang, R. Janisch, G.K. Madsen, and R. Drautz, *Acta Mater.* 115, 259 https://doi.org/10.1016/j.actamat.2016.04.058 (2016).
65. C. Jiang, B. Uberuaga, and S. Srinivasan, *Acta Mater.* 56, 3236 https://doi.org/10.1016/j.actamat.2008.03.012 (2008).
66. E.J. McEniry, T. Hickel, and J. Neugebauer, *Acta Mater.* 150, 53 https://doi.org/10.1016/j.actamat.2018.03.005 (2018).
67. C. Jiang, S. Srinivasan, A. Caro, and S. Maloy, *J. Appl. Phys.* 103, 043502 https://doi.org/10.1063/1.2884529 (2008).
68. M. Nikolussi, et al., *Scr. Mater.* 59, 814 https://doi.org/10.1016/j.scriptamat.2008.06.015 (2008).
69. I. Wood, et al., *J. Appl. Crystallogr.* 37, 82 https://doi.org/10.1107/S0021889803024695 (2004).
70. L. Ventelon, et al., *Phys. Rev. B* 91, 220102 https://doi.org/10.1103/PhysRevB.91.220102 (2015).
71. B. Lüthi, L. Ventelon, C. Elsässer, D. Rodney, and F. Willaime, *Modell. Simul. Mater. Sci. Eng.* 25, 084001 https://doi.org/10.1088/1361-651X/aa88eb (2017).
72. G. Hachet, D. Caillard, L. Ventelon, and E. Clouet, *Acta Mater.* 222, 117440 https://doi.org/10.1016/j.actamat.2021.117440 (2022).
73. S.S. Sarangi and A.K. Kanjarla, *Mater. Today Commun.* 31, 103285 https://doi.org/10.1016/j.mtcomm.2022.103285 (2022).
74. B. Lüthi, L. Ventelon, D. Rodney, and F. Willaime, *Comput. Mater. Sci.* 148, 21 https://doi.org/10.1016/j.commatsci.2018.02.016 (2018).
75. A. Stukowski, V.V. Bulatov, and A. Arsenlis, *Modell. Simul. Mater. Sci. Eng.* 20, 085007 https://doi.org/10.1088/0965-0393/20/8/085007 (2012).
76. L. Ventelon, et al., *Acta Mater.* 247, 118716 https://doi.org/10.1016/j.actamat.2023.118716 (2023).
77. S. Hirayama, et al., *Nucl. Mater. Energy* 31, 101179 https://doi.org/10.1016/j.nme.2022.101179 (2022).
78. K. Kawakami and T. Matsumiya, *ISIJ Int.* 53, 709 https://doi.org/10.2355/isijinternational.53.709 (2013).
79. B. Zhang, et al., *Nat. Commun.* 13, 1 https://doi.org/10.1038/s41467-022-31665-x (2022).
80. A. Nagao, M. Dadfarnia, B.P. Somerday, P. Sofronis, and R.O. Ritchie, *J. Mech. Phys. Solids* 112, 403 https://doi.org/10.1016/j.jmps.2017.12.016 (2018).
81. W. Geng, V. Wang, J.X. Li, N. Ishikawa, H. Kimizuka, K. Tsuzaki, and S. Ogata, *Scripta Mater.* 149, 79 https://doi.org/10.1016/j.scriptamat.2018.02.025 (2018).
82. J.-H. Shim, S.C. Kwon, W.W. Kim, and B.D. Wirth, *J. Nucl. Mater.* 367, 292 https://doi.org/10.1016/j.jnucmat.2007.03.005 (2007).